

<https://doi.org/10.1038/s43246-024-00461-z>

# Emergence of quantum confinement in topological kagome superconductor $\text{CsV}_3\text{Sb}_5$

Check for updates

Yongqing Cai<sup>1,2,12</sup>, Yuan Wang<sup>1,12</sup>, Zhanyang Hao<sup>1,12</sup>, Yixuan Liu<sup>1,12</sup>, Xuelei Sui<sup>3,4</sup>, Zuwei Liang<sup>5</sup>, Xiao-Ming Ma<sup>1</sup>, Fayuan Zhang<sup>1</sup>, Zecheng Shen<sup>1</sup>, Chengcheng Zhang<sup>1</sup>, Zhicheng Jiang<sup>6,7</sup>, Yichen Yang<sup>6,7</sup>, Wanling Liu<sup>6,7</sup>, Qi Jiang<sup>6,7</sup>, Zhengtai Liu<sup>6,7</sup>, Mao Ye<sup>6,7</sup>, Dawei Shen<sup>6,7</sup>, Han Gao<sup>8</sup>, Hanbo Xiao<sup>8</sup>, Zhongkai Liu<sup>8</sup>, Zhe Sun<sup>9</sup>, Yi Liu<sup>9</sup>, Shengtao Cui<sup>9</sup>, Jiabin Chen<sup>4</sup>, Le Wang<sup>1</sup>, Cai Liu<sup>1</sup>, Junhao Lin<sup>1</sup>, Bing Huang<sup>4</sup>, Zhenyu Wang<sup>5</sup>, Xianhui Chen<sup>5</sup>, Jia-Wei Mei<sup>1</sup> ✉, Jianfeng Wang<sup>4,10</sup> ✉ & Chaoyu Chen<sup>1,11</sup> ✉

Quantum confinement is a restriction on the motion of electrons in a material to specific region, resulting in discrete energy levels rather than continuous energy bands. In certain materials, quantum confinement could dramatically reshape the electronic structure and properties of the surface with respect to the bulk. Here, in the recently discovered kagome superconductors  $\text{CsV}_3\text{Sb}_5$ , we unveil the dominant role of quantum confinement in determining their surface electronic structure. Combining angle-resolved photoemission spectroscopy (ARPES) measurement and density-functional theory simulation, we report the observations of two-dimensional quantum well states due to the confinement of bulk electron pocket and Dirac cone to the nearly isolated surface layer. The theoretical calculations on the slab model also suggest that the ARPES observed spectra are almost entirely contributed by the top two layers. Our results not only explain the disagreement of band structures between the recent experiments and calculations, but also suggest an equally important role played by quantum confinement, together with strong correlation and band topology, in shaping the electronic properties of this material.

The observations of superconductivity and chiral charge density wave (CDW) orders in  $\text{AV}_3\text{Sb}_5$  ( $A = \text{K}, \text{Rb}, \text{Cs}$ ) family of materials<sup>1–4</sup> have provoked intensive research interest in condensed matter physics. The critical temperature of superconductivity was found as:  $T_C = 0.93 \text{ K}$  for  $\text{KV}_3\text{Sb}_5$ <sup>5</sup>,  $T_C = 0.92 \text{ K}$  for  $\text{RbV}_3\text{Sb}_5$ <sup>6</sup>, and  $T_C = 2.5 \text{ K}$  for  $\text{CsV}_3\text{Sb}_5$ <sup>2</sup>, respectively. Meanwhile, a chiral CDW order was observed at  $T \sim 80 - 103 \text{ K}$ <sup>1–8</sup>, whose relationship with superconductivity is still under debate<sup>9–15</sup>. Recent experimental and theoretical works have suggested the unconventional nature of both orders<sup>9–17</sup>. While the nature and relationship between these two orders are under active investigations, the nontrivial band topology is certainly playing a fundamental role. Recently, signatures of current flux, especially the resultant time-reversal symmetry breaking (TRSB), have been observed by probes such as scanning tunnelling microscopy (STM)<sup>3</sup>, muon spin relaxation<sup>18,19</sup>, magneto-optical Kerr effect<sup>20</sup>, and electronic magnetochiral anisotropy<sup>21</sup>. However, there are also other experiments reporting sample-dependent signatures of TRSB or even negative evidence<sup>22–25</sup>.

Partially inspired by their  $2 \times 2 \times 2$  or  $2 \times 2 \times 4$  CDW order<sup>7,26</sup>, the experimental studies on the electronic structures of this family have been mainly concentrated on the CDW gap and van Hove singularities (VHSs)<sup>2,12,27–35</sup>. General agreement has been reached on the formation of momentum-dependent CDW gaps<sup>12,27,29,33</sup> as directly measured by angle-resolved photoemission spectroscopy (ARPES). Concerning the VHSs, while several ARPES works have reported the existence of multiple VHSs around the  $\bar{M}$  point with pure or mixed sublattice nature<sup>28,31,32</sup>, such observations are only partially in line with the density-functional theory (DFT) calculations<sup>36,37</sup>. To be specific, DFT has predicted two VHSs in a narrow energy region ( $< 200 \text{ meV}$ ) below the Fermi level at the  $\bar{M}$  point of bulk but no VHS in the same energy window at the  $\bar{L}$  point because of a clear  $k_z$  dispersion along  $\bar{M} - \bar{L}$ . The recent ARPES works<sup>28,31,32</sup> have reported the observations of these two VHSs through a conjecture guided by DFT, yet their  $k_z$  information and the band structure at the  $\bar{L}$  point are missing. In fact, most of the ARPES spectra at  $\bar{M}$  are close to the energy bands at the  $\bar{L}$

A full list of affiliations appears at the end of the paper. ✉ e-mail: [meijw@sustech.edu.cn](mailto:meijw@sustech.edu.cn); [wangjf06@buaa.edu.cn](mailto:wangjf06@buaa.edu.cn); [chency@sustech.edu.cn](mailto:chency@sustech.edu.cn)

point of bulk rather than the M point predicted by DFT calculations. Such disagreement between experiment and theory not only calls for a systematic ARPES experiment to examine the  $k_z$  dispersion, but also an alternative picture to correctly understand the observed electronic structures.

In this work, we report a quantum confinement phenomenon at the surface of kagome superconductor  $\text{CsV}_3\text{Sb}_5$ , which can fully account for the observed spectral features, including the lack of  $k_z$  dispersion as discussed above, and the emergence of quantum well states which we discovered for the first time in this family. Through systematic photon energy-dependent ARPES measurements, we observe a weak but periodic  $k_z$  dispersion along the  $\Gamma - A$  direction but absence of  $k_z$  dispersion along the  $M - L$  and  $K - H$  directions. This causes the results that the measured ARPES spectra along both  $K - M - K$  and  $H - L - H$  look almost identical to the DFT calculated bands along  $H - L - H$ . Furthermore, a clear band splitting is observed for the electron pocket at  $\bar{\Gamma}$ , leading to a subband with pure 2D nature. Both of these features suggest the formation of quantum well states due to the confinement of bands on the surface. Simulated by a slab model with 6 layers of  $\text{CsV}_3\text{Sb}_5$ , all the ARPES spectral features can be captured by our DFT calculations considering the surface relaxation effect. It is found that the interlayer spacing between the topmost and the second kagome layers is increased, which results in a nearly isolated surface layer and the 2D band structure. The ARPES spectra are thus mainly composed of the quantum well states residing on the top two kagome layers. Our results unveil the dominant role of quantum confinement, together with strong correlation and band topology, in shaping the electronic properties of this material.

## Results

High-quality  $\text{CsV}_3\text{Sb}_5$  single crystals are grown by the self-flux method (Methods section), exhibiting a CDW transition at  $T \sim 94$  K and superconductivity at  $T \sim 2.5$  K as demonstrated by our resistivity, heat capacity and magnetization measurements (Supplementary Note 1 and Supplementary Fig. 1). We first present the comparison between the ARPES spectra and DFT calculated band structures of bulk, and show their main disagreements as encountered in most recent works. Taking  $\text{CsV}_3\text{Sb}_5$  as an example, photon energy-dependent ARPES measurements have been performed. According to the periodic spectral intensity variation of energy

distribution curves (EDCs) at the  $\bar{\Gamma}$  point, the high-symmetry points  $\Gamma$  and A of bulk are determined, which correspond to photon energies of 83 eV (Fig. 1a) and 70 eV (Fig. 1e), respectively. For the band structures calculated by slab or measured at a random photon energy, we use  $\bar{\Gamma}$ ,  $\bar{K}$  and  $\bar{M}$  to represent the high symmetry points in the 2D Brillouin zone. Experimental and calculated electronic structures are compared at the  $\Gamma - M - K$  plane (Fig. 1a–d) and  $A - L - H$  plane (Fig. 1e–h). For the DFT calculated Fermi surfaces, clear differences can be seen at the  $\Gamma - M - K$  and  $A - L - H$  planes. For example, while the  $A - L - H$  Fermi surface (Fig. 1f) shows closed loops surrounding the bulk H point, they expand in the  $\Gamma - M - K$  plane, merging with each other and forming a closed loop surrounding the bulk  $\Gamma$  point (Fig. 1b). The tiny loops surrounding the bulk L point (Fig. 1f) are absent at the bulk M point (Fig. 1b). In sharp contrast, despite some intensity variation, the ARPES measured Fermi surfaces are almost identical to each other at both the  $\Gamma - M - K$  (Fig. 1a) and  $A - L - H$  (Fig. 1e) planes, both of which are close to the DFT calculated one at the  $A - L - H$  plane (Fig. 1f).

Such differences between ARPES measurements and DFT calculations can be also reflected by the band structures along high-symmetry lines. According to DFT results, there is a small gap between conduction and valence bands at the bulk M point (dashed box in Fig. 1d), while two conduction and one valence bands cross with each other near the Fermi level around the bulk L point (dashed box in Fig. 1h). In particular, the outer conduction band centered at L crosses one branch of the upper Dirac cone centered at H, forming a new Dirac node almost at the Fermi level. This DFT predicted  $k_z$  dependence along  $M - L$  is missing in the ARPES results, as one can see that both ARPES spectra along  $\Gamma - K - M$  (Fig. 1c) and  $A - H - L$  (Fig. 1g) show very similar features. The Dirac nodes at the Fermi level as discussed above can be clearly observed in both ARPES spectra along  $K - M$  and  $H - L$ . In summary, the DFT calculations on the bulk  $\text{CsV}_3\text{Sb}_5$  predict a clear  $k_z$  dispersion along  $M - L$ , but ARPES results around the  $\bar{M}$  point are  $k_z$  independent, with spectral features almost identical to the DFT calculated results around the bulk L point.

We then move to the electron pocket around the  $\bar{\Gamma}$  point. Before discussing its  $k_z$  dispersion, we will study its detailed band structure based on the high-quality ARPES data we could achieve in this family of materials.

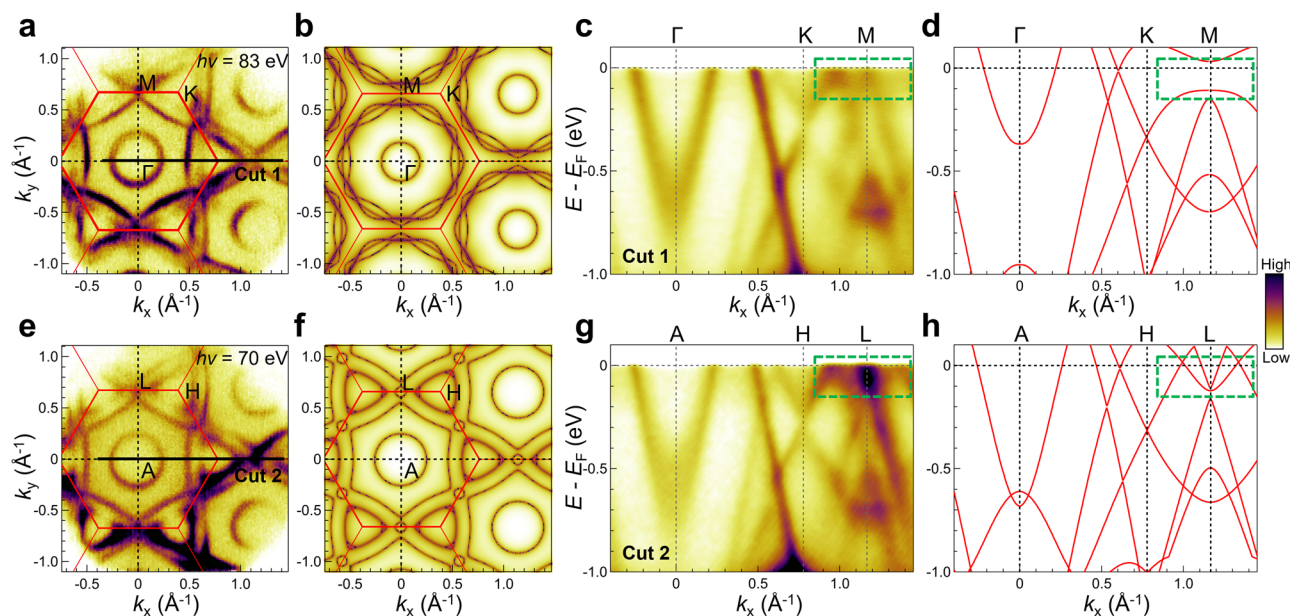


**Fig. 1 | Comparison between ARPES measurements and DFT calculated band structures of  $\text{CsV}_3\text{Sb}_5$ .** **a** Fermi surface mapping of  $\text{CsV}_3\text{Sb}_5$  measured with photon energy  $h\nu = 83$  eV, which corresponds to  $k_z = 7 * 2\pi/c$  plane. **b** DFT calculated constant energy contour (CEC) at  $k_z = 0$  plane. **c** ARPES spectra measured along

$\Gamma - K - M$  as indicated in (a) by the black solid line. **d** DFT calculated band structure along the  $\Gamma - K - M$  direction. **e-h** Same as (a–d) but measured at  $k_z = 6.5 * 2\pi/c$  (photon energy  $h\nu = 70$  eV) and calculated at  $k_z = \pi/c$  plane, respectively. The hexagonal Brillouin zones are marked by the red solid lines.

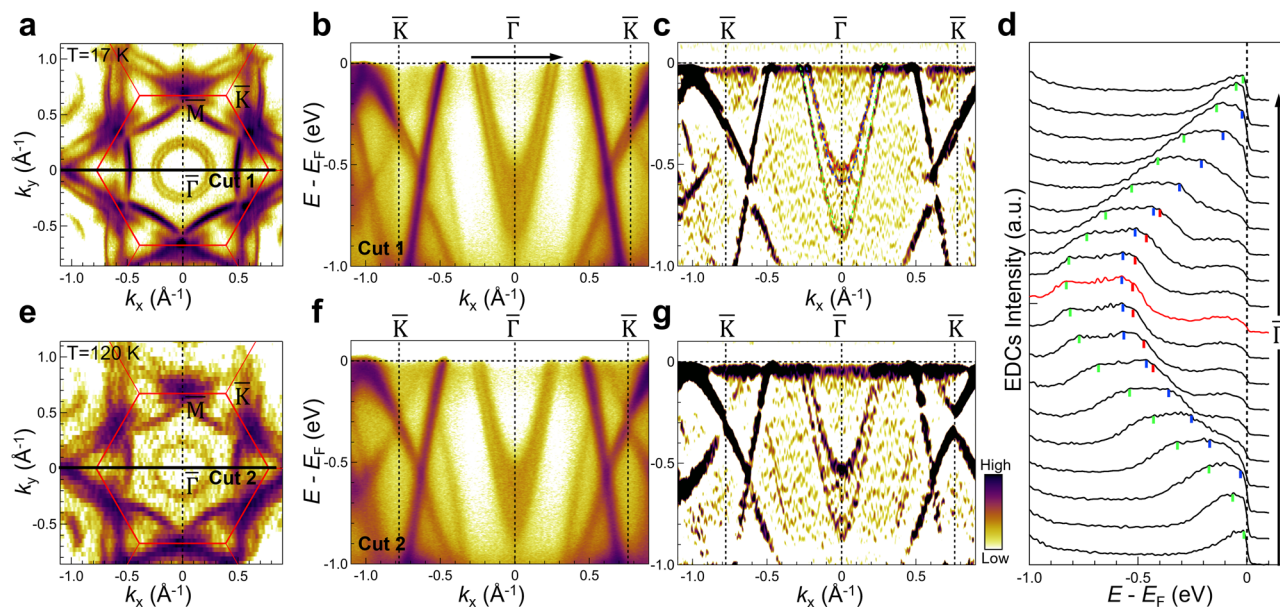


**Fig. 2 | Emergence of quantum well states from the electron pocket at  $\bar{\Gamma}$ .** **a** Fermi surface mapping of  $\text{CsV}_3\text{Sb}_5$  measured with 77 eV photons at 17 K. **b** Band structure measured along the  $\bar{\Gamma} - \bar{K}$  direction marked in (a) by the black solid line. **c** The second derivative image of **b**. **d** EDCs stack plot of (b) with the black arrows in (b)

and (d) marking the momentum region and direction. Red, blue, and green tips mark the peak position of the three bands around  $\bar{\Gamma}$  that are also plotted in (c) by the red, blue and green dashed lines. **e–g** Same as **a–c** but measured at 120 K, above the CDW transition temperature.

Figure 2 presents the ARPES results measured by a general photon energy (77 eV). Different from the single electron pocket predicted by DFT (Fig. 1b, d, f, h), the ARPES results show two circles around  $\bar{\Gamma}$  at the Fermi surface (Fig. 2a), two main electron-like bands crossing the Fermi level along the high-symmetry cut  $\bar{\Gamma} - \bar{K}$  (Fig. 2b, c), and multiple EDC peaks in the corresponding energy-momentum window. These features of multiple bands seem to be the quantized subbands of the bulk electron pocket, which are reminiscent of the quantum well states observed in topological insulators<sup>38–41</sup>.

Other trivial scenarios may also account for band duplicates. The first one is surface inhomogeneity, which could lead to multiple sets of bands from different domains. This is not the present case as the subbands observed here are all symmetric with respect to  $\bar{\Gamma}$ , and not all the main bands have replicas (see more details in Supplementary Note 2 and Supplementary Fig. 2). The second possibility is superlattice bands induced by CDW, which can be also ruled out as these subbands are still present above the CDW transition temperature (Fig. 2e–g). The third one is caused by  $k_z$  projection, in which the minimum and maximum edge of band continuum along  $k_z$  contribute two band-like features in ARPES spectra<sup>42</sup>. Such features have indeed been captured in recent ARPES measurement from this family of materials<sup>27–29</sup>. According to the available data<sup>27</sup>, split bands of the  $\bar{\Gamma}$  electron pocket from  $k_z$  projection have different in-plane dispersion curvature (e.g., effective mass) (Supplementary Fig. 3). However, the split bands we observed here (Fig. 2b, c, f, g) are almost shifted rigidly to each other. Furthermore, the number of split bands we find here is more than just two (Fig. 2c, d and Supplementary Fig. 4). Both features suggest that  $k_z$  projection is unlikely the reason of our case. Other possibilities such as polaronic effect<sup>43,44</sup> can also be excluded since these split bands cross the Fermi level. The above analyses strongly point to quantum well states as the origin of these split bands.

The definitive evidence of quantum well states come from the (quasi-) 2D nature of the split subbands. In Fig. 3a, we show the photon energy-dependent spectra, corresponding to 8 consecutive  $k_z$  values between  $k_z = 6.5 * 2\pi/c$  and  $k_z = 7.0 * 2\pi/c$ . The most striking feature is the outermost electron-like band as highlighted by the green dashed lines. At the first glance, this electron band shows no detectable change with  $k_z$ . By detailed analysis, the band bottom and Fermi vectors all present flat dispersion with  $k_z$ , as demonstrated in Fig. 3b, c, respectively.

This clearly proves the outermost subband as a surface quantum well state. Concerning the inner electron subband, the same analyses presented in Fig. 3a, b unveil its  $k_z$  dependence with a band width  $\sim 100$  meV. However, this  $k_z$  dispersion is much weaker than the bulk band ( $\sim 400$  meV) calculated by DFT. It suggests that besides the bulk nature, the inner subband also shares a similar origin of quantum confinement, but its confinement is weaker than that of the outermost band. Nevertheless, the different  $k_z$  dependence between the outermost and inner bands suggests that they are not from  $k_z$  projection of the same bulk band. In addition, a swapped intensity is observed between the two  $k_z$  projected subbands under different photon energies<sup>31</sup>, while for ours, the outer band always has the highest intensity. We assume that the discrepancies on the  $k_z$  dependence may be attributed to differences in the terminations measured by ARPES (see more details in Supplementary Note 3 and Supplementary Figs. 5 and 6). Our ARPES measurements indicate that a well potential may be formed on the surface.

To demonstrate the origin of this quantum confinement, we build a symmetric slab model consisting of six  $\text{Cs-Sb}_2\text{-V/Sb}_1\text{-Sb}_2$  layers of  $\text{CsV}_3\text{Sb}_5$  with Cs atomic layers at both terminations (upper panel of Fig. 4a). The (0001) surface of  $\text{CsV}_3\text{Sb}_5$  belongs to a polar surface. In general, a stable polar surface of solid is often accompanied by large structural relaxation or surface reconstruction<sup>45</sup>. Our DFT calculations reveal that the structural relaxations mainly occur at the surface layers of  $\text{CsV}_3\text{Sb}_5$  (Supplementary Fig. 7). The topmost  $\text{Cs-Sb}_2\text{-V/Sb}_1\text{-Sb}_2$  unit-cell (UC) layer is found far away from the UC layers below, and atomic-layer spacing inside this topmost UC layer is reduced, which leads to the surface UC layer of  $\text{CsV}_3\text{Sb}_5$  relatively free-standing. In contrast, the relaxation effect of inner UC layers is negligible, and they almost keep the bulk structure nature. In the lower panel of Fig. 4a, we plot the average local potential on each  $\text{CsV}_3\text{Sb}_5$  UC layer along the  $z$  direction of slab. Remarkably, a potential drop ( $\sim 1$  eV) occurs at the surface due to the relaxation, which causes the formation of a quantum confinement near the surface. In Fig. 4b, c, we present the DFT calculated band structures of slab with projections onto the topmost UC layer and the top two UC layers, respectively. By comparing with ARPES results (Fig. 4d), the following relevant messages can be obtained. First, the pure surface quantum well state (the outermost electron band) is almost entirely contributed by the topmost  $\text{CsV}_3\text{Sb}_5$  UC layer (Fig. 4b), confirming its origin of quantum confinement. Second, just using the DFT calculated bands from



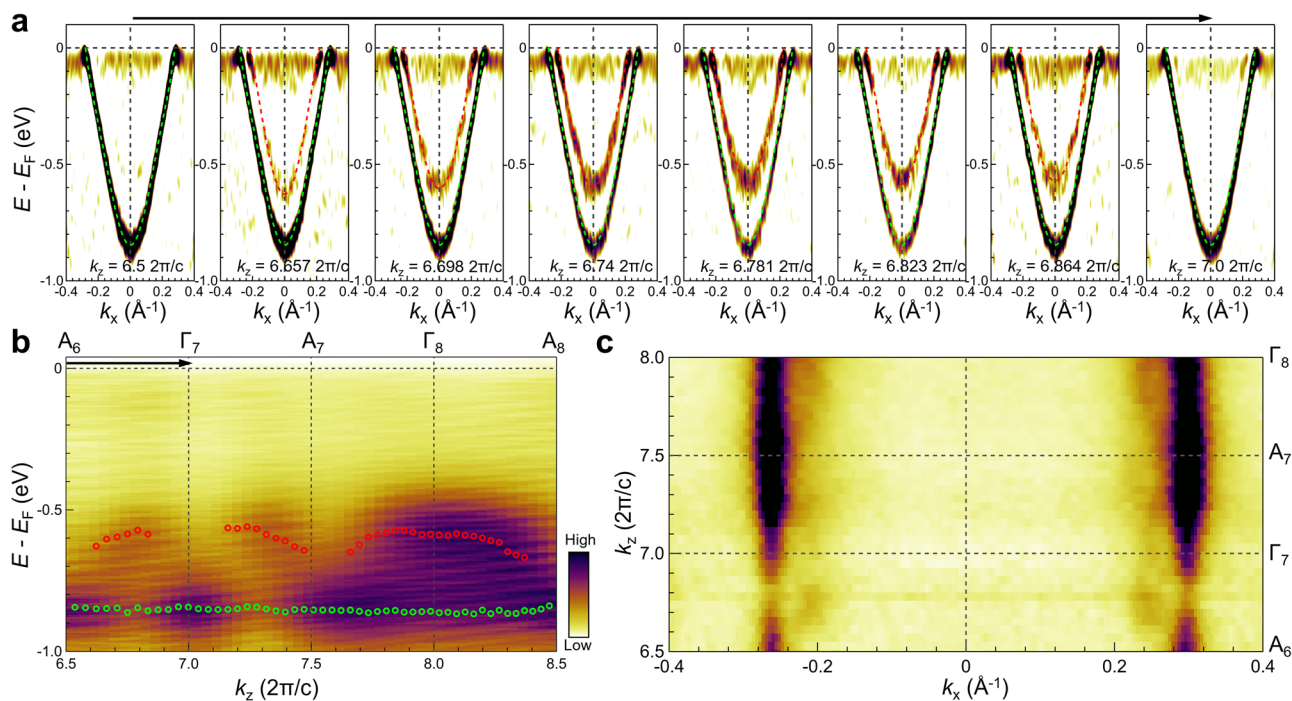


**Fig. 3 |  $k_z$  dispersion of the quantum well states.** **a** Band structure around Brillouin zone center  $\bar{\Gamma}$  under a series of photon energies. Main subbands are labeled by the red and green dashed lines, in the same way as in Fig. 2c. **b** Photon energy-dependent spectra for photoemission intensity at the Brillouin zone center. Open circles

represent the binding energy evolution of the corresponding subbands in **a**. **c** ARPES spectral intensity map around the Fermi level in  $k_x - k_z$  plane. The two strong linear features correspond to the Fermi momenta of the outer subband.

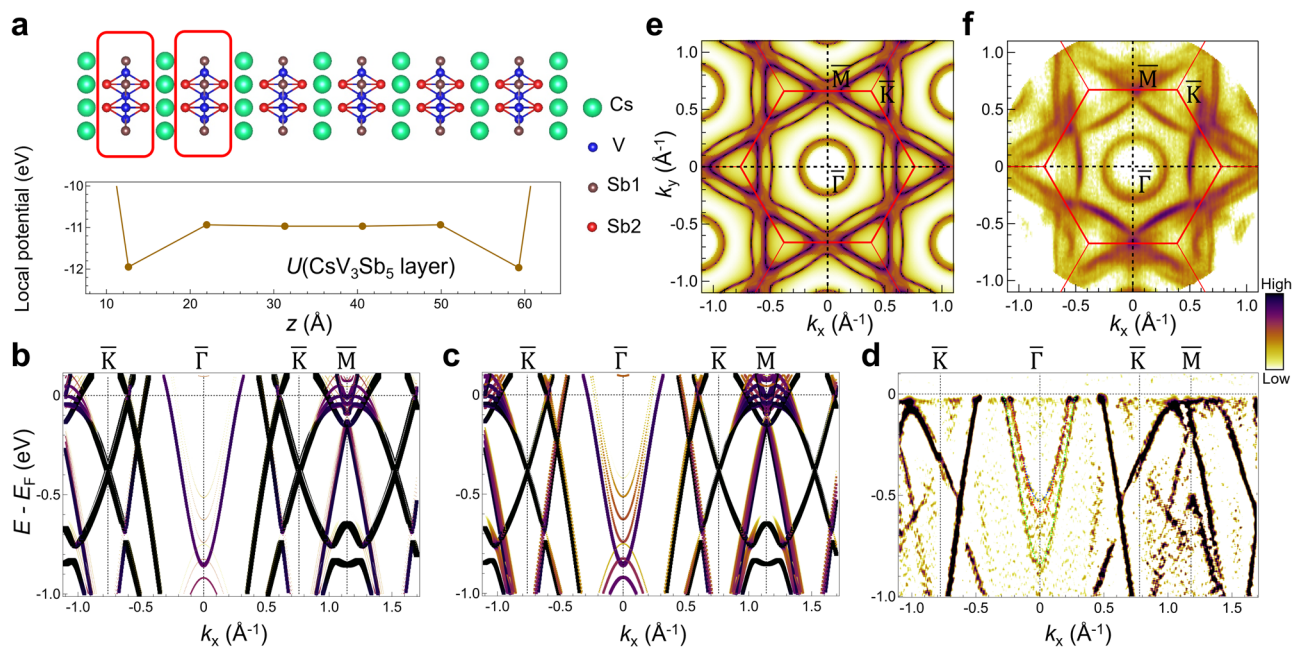


**Fig. 4 | Surface relaxation effect on the formation of quantum well states.** **a** Upper panel: schematic of slab structure consisting of six layers of  $\text{CsV}_3\text{Sb}_5$ . Lower panel: average local potential on each  $\text{CsV}_3\text{Sb}_5$  unit-cell (UC) layer along the  $z$  direction of slab after surface relaxation. **b-d** Comparison of calculated and measured band

structures along the  $\bar{K} - \bar{\Gamma} - \bar{K}$  direction. In **b** and **c**, the simulated band structures are projected to the topmost layer and the top two layers, respectively. In **d**, the ARPES data was measured using 77 eV photon energy, same as that in Fig. 2. **e, f** Comparison of calculated and measured Fermi surfaces.

the contributions of the top two UC layers of a 6-layer slab is enough to simulate the ARPES spectra satisfactorily (Fig. 4c), in agreement with the ARPES probe depth ( $1 \sim 2 \text{ nm}$ ) within the photon energy range reported. This indicates that the ARPES observed spectra are almost of surface origin, providing consistent explanation for the lack of  $k_z$  dispersion at the  $\bar{K}$  and  $\bar{M}$

points, as well as the weak  $k_z$  dependence of the inner electron band at  $\bar{\Gamma}$ . Employing the slab model of  $\text{CsV}_3\text{Sb}_5$ , the calculated Fermi surface by projection to the top two UC layers is shown in Fig. 4e, which is in good agreement with the experimental measurements (Fig. 4f) using a general photon energy. Importantly, this Fermi surface is nearly  $k_z$  independent due

to the (quasi-) 2D nature of bands, significantly different from the cases shown in Fig. 1b, f.

## Discussion

Spontaneous TRSB orders have long been sought in many quantum systems<sup>46–50</sup>. Recent theoretical efforts<sup>37,51–54</sup> suggested that the chiral flux phase is the lowest energy state of  $2 \times 2$  CDW in CsV<sub>3</sub>Sb<sub>5</sub> family, which naturally gives rise to TRSB. Pioneering muon spin rotation measurements on this family have reported the evidence of TRSB chiral flux phase<sup>18,55</sup> but controversies remain. On the one hand, there are conflicting experimental results concerning the concurrence of TRSB<sup>18,24,25,56</sup> and the chirality of the  $2 \times 2$  CDW<sup>3,22,23,57</sup>, rendering the nature of CDW and its relationship with chiral flux phase unclear. On the other hand, no indication of chiral flux current can be found from spin-polarized STM measurement<sup>22</sup>. Our findings suggest that these controversies might come from the layer-dependent CDW instability due to the quantum confinement and surface relaxation as we revealed.

Our DFT calculations further prove that the CDW instability is layer-dependent. The surface (top/bottom) UC layer has significantly less phonon softening than the inner UC layer (Supplementary Fig. 8a), indicating that the surface CDW instability is less favorable. The tri-hexagonal reconstruction is obvious for the inner UC layer, while almost invisible for the surface UC layer of the relaxed slab (Supplementary Fig. 8b). The corresponding unfolded band structure projected to the top/bottom UC layer (Supplementary Fig. 8e) resembles with the unreconstructed one (Supplementary Fig. 8c), e.g., the Dirac nodes surrounding K remain intact. In contrast, these Dirac nodes projected to the inner UC layer are gapped by the reconstruction (Supplementary Fig. 8f). These results suggest that quantum confinement and surface relaxation lead to much weaker CDW instability on the surface. Together with the much reduced interlayer coupling (See Fig. 4a), these effects make the proposed interlayer coupled chiral flux phase<sup>52</sup> unfavorable. This potentially explains why bulk sensitive probes such as muon spin rotation<sup>18</sup>, optical Kerr rotation<sup>56</sup>, and electronic magnetochiral anisotropy<sup>21</sup> give positive evidences of TRSB, while the surface sensitive probe such as spin-polarized STM<sup>22</sup> could not detect any signature of spin texture corresponding to the chiral flux phase. Consequently, quantum confinement and surface relaxation provide active ingredient to understand the surface-related, controversial phenomena in this family.

## Methods

### Sample growth and characterization

KV<sub>3</sub>Sb<sub>5</sub> and CsV<sub>3</sub>Sb<sub>5</sub> single crystals were grown by the self-flux method. High purity K and Cs (clump), V (powder) and Sb (ball) in the ratio of 2:1:6 were placed in an alumina crucible. The crucible was then double sealed into an evacuated quartz tube under a pressure of  $10^{-6}$  Torr to prevent the assembly from reacting with air during the reaction. The quartz tube containing the alumina crucible was placed in the furnace and the temperature was increased to 500 °C in 5 h. The mixtures were kept in 500 °C for 10 h. Then the quartz tube was heated at 1050 °C for 12 hours, after this, the quartz tube was cooled to 650 °C very slowly. After the heat treatment, the quartz tube was removed and centrifuged. A large number of millimeter-sized hexagonal KV<sub>3</sub>Sb<sub>5</sub> and CsV<sub>3</sub>Sb<sub>5</sub> single crystals were obtained.

### Transport, heat capacity, and magnetic measurements

Resistivity and heat capacity were measured by Physical Property Measurement System (PPMS, Quantum Design). To characterize the resistivity, a standard four-probe method was employed with a probe current of 0.5 mA in the *ab* plane of the crystals. And to measure the heat capacity, several flat crystals of approximate 1.5 mm size were selected, and Apejion N-grease was used to ensure the connection with heat capacity stage. Magnetization measurements were performed by Magnetic Property Measurement System (MPMS3, Quantum Design). Quartz paddle was used, and the magnetic field was perpendicular to *c*-axis to minimize the diamagnetic contribution.

## ARPES measurement

ARPES measurements were performed at the BL03U beamline of the Shanghai Synchrotron Radiation Facility (SSRF) and beamline 13U of the National Synchrotron Radiation Laboratory (NSRL). The energy resolution was set at 15 meV for Fermi surface mapping and 7.5 meV for band structure measurements. The angular resolution was set at 0.1°. Most samples were cleaved in situ under ultra-high vacuum conditions with pressure better than  $5 \times 10^{-11}$  mbar and temperatures below 20 K, while some samples were cleaved above 120 K.

## First-principles calculations

The first-principles calculations are performed using the Vienna ab initio simulation package<sup>58</sup> within the projector augmented wave method<sup>59</sup> and the generalized gradient approximation of the Perdew-Burke-Ernzerhof<sup>60</sup> exchange-correlation functional. The plane-wave basis with an energy cutoff of 400 eV is adopted. To simulate the surface structures, the slab model is built, and the thickness of vacuum is taken to be 16 Å. *Γ*-centered  $12 \times 12 \times 6$  *k*-point meshes and  $12 \times 12 \times 1$  *k*-point meshes are adopted for bulk and slab structures respectively. Employing the experimental lattice constants of  $a = b = 5.495$  Å (and  $c = 9.308$  Å for bulk), the crystal and slab structures of CsV<sub>3</sub>Sb<sub>5</sub> is relaxed with van der Waals correction<sup>61</sup> until the residual forces on each atom is less than 0.005 eV/Å.

## Data availability

The main data supporting the conclusions of this study are available within the paper and its Supplementary Material. Additional data can be obtained from the corresponding authors upon request.

Received: 4 November 2023; Accepted: 19 February 2024;

Published online: 13 March 2024

## References

- Ortiz, B. R. et al. New kagome prototype materials: discovery of KV<sub>3</sub>Sb<sub>5</sub>, RbV<sub>3</sub>Sb<sub>5</sub>, and CsV<sub>3</sub>Sb<sub>5</sub>. *Phys. Rev. Mater.* **3**, 094407 (2019).
- Ortiz, B. R. et al. CsV<sub>3</sub>Sb<sub>5</sub>: A Z2 topological kagome metal with a superconducting ground state. *Phys. Rev. Lett.* **125**, 247002 (2020).
- Jiang, Y. X. et al. Unconventional chiral charge order in kagome superconductor KV<sub>3</sub>Sb<sub>5</sub>. *Nat. Mater.* **20**, 1353–1357 (2021).
- Yang, S.-Y. et al. Giant, unconventional anomalous Hall effect in the metallic frustrated magnet candidate, KV<sub>3</sub>Sb<sub>5</sub>. *Sci. Adv.* **6**, eabb6003 (2020).
- Ortiz, B. R. et al. Superconductivity in the Z2 kagome metal KV<sub>3</sub>Sb<sub>5</sub>. *Phys. Rev. Mater.* **5**, 034801 (2021).
- Yin, Q. et al. Superconductivity and normal-state properties of kagome metal RbV<sub>3</sub>Sb<sub>5</sub> single crystals. *Chin. Phys. Lett.* **38**, 037403 (2021).
- Li, H. et al. Observation of unconventional charge density wave without acoustic phonon anomaly in kagome superconductors AV<sub>3</sub>Sb<sub>5</sub> (A=Rb, Cs). *Phys. Rev. X* **11**, 031050 (2021).
- Liang, Z. et al. Three-dimensional charge density wave and surface-dependent vortex-core states in a kagome superconductor CsV<sub>3</sub>Sb<sub>5</sub>. *Phys. Rev. X* **11**, 031026 (2021).
- Du, F. et al. Pressure-induced double superconducting domes and charge instability in the kagome metal KV<sub>3</sub>Sb<sub>5</sub>. *Phys. Rev. B* **103**, L220504 (2021).
- Song, Y. et al. Competition of superconductivity and charge density wave in selective oxidized CsV<sub>3</sub>Sb<sub>5</sub> thin flakes. *Phys. Rev. Lett.* **127**, 237001 (2021).
- Xu, H.-S. et al. Multiband superconductivity with sign-preserving order parameter in kagome superconductor CsV<sub>3</sub>Sb<sub>5</sub>. *Phys. Rev. Lett.* **127**, 187004 (2021).
- Lou, R. et al. Charge-density-wave-induced peak-dip-hump structure and the multiband superconductivity in a kagome superconductor CsV<sub>3</sub>Sb<sub>5</sub>. *Phys. Rev. Lett.* **128**, 036402 (2022).

13. Zhao, C. C. et al. Nodal superconductivity and superconducting domes in the topological Kagome metal CsV<sub>3</sub>Sb<sub>5</sub>. *arXiv* <https://doi.org/10.48550/arXiv.2102.08356> (2021).
14. Chen, K. Y. et al. Double Superconducting Dome and Triple Enhancement of T<sub>c</sub> in the Kagome Superconductor CsV<sub>3</sub>Sb<sub>5</sub> under High Pressure. *Phys. Rev. Lett.* **126**, 247001 (2021).
15. Song, B. et al. Anomalous enhancement of charge density wave in kagome superconductor CsV<sub>3</sub>Sb<sub>5</sub> approaching the 2D limit. *Nat. Commun.* **14**, 2492 (2023).
16. Wang, Z. et al. Electronic nature of chiral charge order in the kagome superconductor CsV<sub>3</sub>Sb<sub>5</sub>. *Phys. Rev. B* **104**, 075148 (2021).
17. Chen, H. et al. Roton pair density wave in a strong-coupling kagome superconductor. *Nature* **599**, 222–228 (2021).
18. Mielke, C. 3rd et al. Time-reversal symmetry-breaking charge order in a kagome superconductor. *Nature* **602**, 245–250 (2022).
19. Guguchia, Z. et al. Tunable unconventional kagome superconductivity in charge ordered RbV<sub>3</sub>Sb<sub>5</sub> and KV<sub>3</sub>Sb<sub>5</sub>. *Nat. Commun.* **14**, 153 (2023).
20. Xu, Y. et al. Three-state nematicity and magneto-optical Kerr effect in the charge density waves in kagome superconductors. *Nat. Phys.* **18**, 1470–1475 (2022).
21. Guo, C. et al. Switchable chiral transport in charge-ordered kagome metal CsV<sub>3</sub>Sb<sub>5</sub>. *Nature* **611**, 461–466 (2022).
22. Li, H. et al. No observation of chiral flux current in the topological kagome metal CsV<sub>3</sub>Sb<sub>5</sub>. *Phys. Rev. B* **105**, 045102 (2022).
23. Li, H. et al. Rotation symmetry breaking in the normal state of a kagome superconductor KV<sub>3</sub>Sb<sub>5</sub>. *Nat. Phys.* **18**, 265–270 (2022).
24. Farhang, C. et al. Unconventional specular optical rotation in the charge ordered state of Kagome metal CsV<sub>3</sub>Sb<sub>5</sub>. *Nat. Commun.* **14**, 5326 (2023).
25. Saykin, D. R. et al. High resolution polar Kerr effect studies of CsV<sub>3</sub>Sb<sub>5</sub>: tests for time-reversal symmetry breaking below the charge-order transition. *Phys. Rev. Lett.* **131**, 016901 (2023).
26. Ortiz, B. R. et al. Fermi Surface Mapping and the Nature of Charge-Density-Wave Order in the Kagome Superconductor CsV<sub>3</sub>Sb<sub>5</sub>. *Phys. Rev. X* **11**, 041030 (2021).
27. Nakayama, K. et al. Multiple energy scales and anisotropic energy gap in the charge-density-wave phase of the kagome superconductor CsV<sub>3</sub>Sb<sub>5</sub>. *Phys. Rev. B* **104**, L161112 (2021).
28. Cho, S. et al. Emergence of New van Hove Singularities in the Charge Density Wave State of a Topological Kagome Metal RbV<sub>3</sub>Sb<sub>5</sub>. *Phys. Rev. Lett.* **127**, 236401 (2021).
29. Liu, Z. et al. Charge-Density-Wave-Induced Bands Renormalization and Energy Gaps in a Kagome Superconductor RbV<sub>3</sub>Sb<sub>5</sub>. *Phys. Rev. X* **11**, 041010 (2021).
30. Hao, Z. et al. Dirac nodal lines and nodal loops in the topological kagome superconductor CsV<sub>3</sub>Sb<sub>5</sub>. *Phys. Rev. B* **106**, L081101 (2022).
31. Hu, Y. et al. Rich nature of Van Hove singularities in Kagome superconductor CsV<sub>3</sub>Sb<sub>5</sub>. *Nat. Commun.* **13**, 2220 (2022).
32. Kang, M. et al. Twofold van Hove singularity and origin of charge order in topological kagome superconductor CsV<sub>3</sub>Sb<sub>5</sub>. *Nat. Phys.* **18**, 301–308 (2022).
33. Luo, H. et al. Electronic nature of charge density wave and electron-phonon coupling in kagome superconductor KV<sub>3</sub>Sb<sub>5</sub>. *Nat. Commun.* **13**, 273 (2022).
34. Nakayama, K. et al. Carrier Injection and Manipulation of Charge-Density Wave in Kagome Superconductor CsV<sub>3</sub>Sb<sub>5</sub>. *Phys. Rev. X* **12**, 011001 (2022).
35. Hu, Y. et al. Topological surface states and flat bands in the kagome superconductor CsV<sub>3</sub>Sb<sub>5</sub>. *Sci. Bull.* **67**, 495–500 (2022).
36. Zhao, J., Wu, W., Wang, Y. & Yang, S. A. Electronic correlations in the normal state of the kagome superconductor KV<sub>3</sub>Sb<sub>5</sub>. *Phys. Rev. B* **103**, L241117 (2021).
37. Tan, H., Liu, Y., Wang, Z. & Yan, B. Charge Density Waves and Electronic Properties of Superconducting Kagome Metals. *Phys. Rev. Lett.* **127**, 046401 (2021).
38. Bianchi, M. et al. Coexistence of the topological state and a two-dimensional electron gas on the surface of Bi<sub>2</sub>Se<sub>3</sub>. *Nat. Commun.* **1**, 128 (2010).
39. Bianchi, M. et al. Simultaneous Quantization of Bulk Conduction and Valence States through Adsorption of Nonmagnetic Impurities on Bi<sub>2</sub>Se<sub>3</sub>. *Phys. Rev. Lett.* **107**, 086802 (2011).
40. Bahramy, M. S. et al. Emergent quantum confinement at topological insulator surfaces. *Nat. Commun.* **3**, 1159 (2012).
41. Chen, C. et al. Robustness of topological order and formation of quantum well states in topological insulators exposed to ambient environment. *Proceedings of the National Academy of Sciences* **109**, 3694–3698 (2012).
42. Hao, Z. et al. Multiple Dirac nodal lines in an in-plane anisotropic semimetal TaNiTe<sub>5</sub>. *Phys. Rev. B* **104**, 115158 (2021).
43. Chen, C. et al. Emergence of Interfacial Polarons from Electron–Phonon Coupling in Graphene/h-BN van der Waals Heterostructures. *Nano Lett* **18**, 1082–1087 (2018).
44. Chen, C. et al. Observation of a two-dimensional liquid of Frohlich polarons at the bare SrTiO<sub>3</sub> surface. *Nat. Commun.* **6**, 8585 (2015).
45. Wang, J. et al. Structural stability and topological surface states of the SnTe (111) surface. *Phys. Rev. B* **89**, 125308 (2014).
46. Raghu, S., Qi, X.-L., Honerkamp, C. & Zhang, S.-C. Topological Mott Insulators. *Phys. Rev. Lett.* **100**, 156401 (2008).
47. Haldane, F. D. M. Model for a Quantum Hall Effect without Landau Levels: Condensed-Matter Realization of the “Parity Anomaly”. *Phys. Rev. Lett.* **61**, 2015–2018 (1988).
48. Zhao, L. et al. Evidence of an odd-parity hidden order in a spin–orbit coupled correlated iridate. *Nat. Phys.* **12**, 32–36 (2015).
49. Varma, C. M. Non-Fermi-liquid states and pairing instability of a general model of copper oxide metals. *Phys. Rev. B* **55**, 14554–14580 (1997).
50. Chakravarty, S., Laughlin, R. B., Morr, D. K. & Nayak, C. Hidden order in the cuprates. *Phys. Rev. B* **63**, 094503 (2001).
51. Park, T., Ye, M. & Balents, L. Electronic instabilities of kagome metals: Saddle points and Landau theory. *Phys. Rev. B* **104**, 035142 (2021).
52. Feng, X., Jiang, K., Wang, Z. & Hu, J. Chiral flux phase in the Kagome superconductor AV<sub>3</sub>Sb<sub>5</sub>. *Sci. Bull.* **66**, 1384–1388 (2021).
53. Feng, X., Zhang, Y., Jiang, K. & Hu, J. Low-energy effective theory and symmetry classification of flux phases on the kagome lattice. *Phys. Rev. B* **104**, 165136 (2021).
54. Lin, Y.-P. & Nandkishore, R. M. Complex charge density waves at Van Hove singularity on hexagonal lattices: Haldane-model phase diagram and potential realization in the kagome metals AV<sub>3</sub>Sb<sub>5</sub> (A = K, Rb, Cs). *Phys. Rev. B* **104**, 045122 (2021).
55. Kenney, E. M. et al. Absence of local moments in the kagome metal KV<sub>3</sub>Sb<sub>5</sub> as determined by muon spin spectroscopy. *J. Phys.: Condens. Matter* **33**, 235801 (2021).
56. Wu, Q. et al. Simultaneous formation of two-fold rotation symmetry with charge order in the kagome superconductor CsV<sub>3</sub>Sb<sub>5</sub> by optical polarization rotation measurement. *Phys. Rev. B* **106**, 205109 (2022).
57. Shumiya, N. et al. Intrinsic nature of chiral charge order in the kagome superconductor RbV<sub>3</sub>Sb<sub>5</sub>. *Phys. Rev. B* **104**, 035131 (2021).
58. Kresse, G. & Furthmüller, J. Efficient iterative schemes for ab initio total-energy calculations using a plane-wave basis set. *Phys. Rev. B* **54**, 11169–11186 (1996).
59. Blöchl, P. E. Projector augmented-wave method. *Phys. Rev. B* **50**, 17953–17979 (1994).
60. Perdew, J. P., Burke, K. & Ernzerhof, M. Generalized Gradient Approximation Made Simple. *Phys. Rev. Lett.* **77**, 3865–3868 (1996).



61. Grimme, S., Antony, J., Ehrlich, S. & Krieg, H. A consistent and accurate ab initio parametrization of density functional dispersion correction (DFT-D) for the 94 elements H-Pu. *J. Chem. Phys.* **132**, 154104 (2010).

## Acknowledgements

This work is supported by the National Key R&D Program of China (Grant No. 2022YFA1403700), the National Natural Science Foundation of China (NSFC) (Grants No. 12074163 and 12004030), Guangdong Basic and Applied Basic Research Foundation (Grants No. 2022B1515020046, 2022B1515130005 and 2021B1515130007), the Guangdong Innovative and Entrepreneurial Research Team Program (Grants No. 2017ZT07C062 and 2019ZT08C044), Shenzhen Science and Technology Program (Grant No. KQTD20190929173815000), Shenzhen Key Laboratory of Advanced Quantum Functional Materials and Devices (ZDSYS20190902092905285), the Fundamental Research Funds for the Central Universities and China Postdoctoral Science Foundation (2020M682780, 2022M711495). The authors acknowledge the assistance of SUSTech Core Research Facilities. The calculations were performed at Tianhe2-JK at Beijing Computational Science Research Center.

## Author contributions

C.C., J.W. and J.M. proposed and designed the research. X.S., J.C., B.H., and J.W. conducted DFT calculations. Z.H., Y.L., L.W. and J.M. contribute to the sample growth. Y.C., Y.W., Z.H., X.M., F.Z., Z.S., C.Z., C.L. and C.C. carried out the ARPES experiments. Z.J., Y.Y., W.L., Q.J., Z.L., M.Y., D.S., H.G., H.X., Z.L., Z.S., Y.L. and S.C. contribute to the development and maintenance of the ARPES systems. Y.C., J.W., and C.C. analyzed the data and wrote the paper. Z.L., J.L., Z.W. and X.C. participated in discussion and comment on the paper.

## Competing interests

The authors declare no competing interests.

## Additional information

**Supplementary information** The online version contains supplementary material available at <https://doi.org/10.1038/s43246-024-00461-z>.

**Correspondence** and requests for materials should be addressed to Jia-Wei Mei, Jianfeng Wang or Chaoyu Chen.

**Peer review information** *Communications Materials* thanks the anonymous reviewers for their contribution to the peer review of this work. Primary Handling Editors: Toru Hirahara and Aldo Isidori. A peer review file is available.

**Reprints and permissions information** is available at <http://www.nature.com/reprints>

**Publisher's note** Springer Nature remains neutral with regard to jurisdictional claims in published maps and institutional affiliations.

**Open Access** This article is licensed under a Creative Commons Attribution 4.0 International License, which permits use, sharing, adaptation, distribution and reproduction in any medium or format, as long as you give appropriate credit to the original author(s) and the source, provide a link to the Creative Commons licence, and indicate if changes were made. The images or other third party material in this article are included in the article's Creative Commons licence, unless indicated otherwise in a credit line to the material. If material is not included in the article's Creative Commons licence and your intended use is not permitted by statutory regulation or exceeds the permitted use, you will need to obtain permission directly from the copyright holder. To view a copy of this licence, visit <http://creativecommons.org/licenses/by/4.0/>.

© The Author(s) 2024

<sup>1</sup>Shenzhen Institute for Quantum Science and Engineering (SIQSE) and Department of Physics, Southern University of Science and Technology (SUSTech), Shenzhen 518055, China. <sup>2</sup>School of Physics, Dalian University of Technology, Dalian 116024, China. <sup>3</sup>College of Mathematics and Physics, Beijing University of Chemical Technology, Beijing 100029, China. <sup>4</sup>Beijing Computational Science Research Center, Beijing 100193, China. <sup>5</sup>Department of Physics and Chinese Academy of Sciences Key laboratory of Strongly-coupled Quantum Matter Physics, University of Science and Technology of China, Hefei, Anhui 230026, China. <sup>6</sup>Shanghai Synchrotron Radiation Facility, Shanghai Advanced Research Institute, Chinese Academy of Sciences, Shanghai 201204, China. <sup>7</sup>Shanghai Institute of Microsystem and Information Technology, Chinese Academy of Sciences, Shanghai 200050, People's Republic of China. <sup>8</sup>School of Physical Science and Technology, ShanghaiTech University, Shanghai 201210, China. <sup>9</sup>National Synchrotron Radiation Laboratory, University of Science and Technology of China, Hefei, Anhui 230029, China. <sup>10</sup>School of Physics, Beihang University, Beijing 100191, China. <sup>11</sup>Institute of Advanced Science Facilities, Shenzhen 518107, China. <sup>12</sup>These authors contributed equally: Yongqing Cai, Yuan Wang, Zhanyang Hao, Yixuan Liu. ✉ e-mail: [meijw@sustech.edu.cn](mailto:meijw@sustech.edu.cn); [wangjf06@buaa.edu.cn](mailto:wangjf06@buaa.edu.cn); [chency@sustech.edu.cn](mailto:chency@sustech.edu.cn)